Accuracy and repeatability of joint sparsity multi-component estimation in MR Fingerprinting

L. Nunez-Gonzalez [a,1], M.A. Nagtegaal [b,1,*], D.H.J. Poot [a], J. de Bresser [c], M.J.P. van Osch [d], J.A. Hernandez-Tamames [a,b], F.M. Vos [a,b]

[a] Department of Radiology and Nuclear Medicine, Erasmus MC, Rotterdam, the Netherlands
[b] Department of Imaging Physics, Delft University of Technology, Delft, the Netherlands
[c] Department of Radiology, Leiden University Medical Center, Leiden, the Netherlands
[d] C.J. Gorter Center for MRI, Radiology Department, Leiden University Medical Center, Leiden, the Netherlands

ARTICLE INFO

ABSTRACT

MR fingerprinting (MRF) is a promising method for quantitative characterization of tissues. Often, voxel-wise measurements are made, assuming a single tissue-type per voxel. Alternatively, the Sparsity Promoting Iterative Joint Non-negative least squares Multi-Component MRF method (SPIJN-MRF) facilitates tissue parameter estimation for identified components as well as partial volume segmentations. The aim of this paper was to evaluate the accuracy and repeatability of the SPIJN-MRF parameter estimations and partial volume segmentations. This was done (1) through numerical simulations based on the BrainWeb phantoms and (2) using *in vivo* acquired MRF data from 5 subjects that were scanned on the same week-day for 8 consecutive weeks. The partial volume segmentations of the SPIJN-MRF method were compared to those obtained by two conventional methods: SPM12 and FSL. SPIJN-MRF showed higher accuracy *in simulations* in comparison to FSL- and SPM12-based segmentations: Fuzzy Tanimoto Coefficients (FTC) comparing these segmentations and Brainweb references were higher than 0.95 for SPIJN-MRF in all the tissues and between 0.6 and 0.7 for SPM12 and FSL in white and gray matter and between 0.5 and 0.6 in CSF. For the *in vivo MRF* data, the estimated relaxation times were in line with literature and minimal variation was observed. Furthermore, the coefficient of variation (CoV) for estimated tissue volumes with SPIJN-MRF were 10.5% for the myelin water, 6.0% for the white matter, 5.6% for the gray matter, 4.6% for the CSF and 1.1% for the total brain volume. CoVs for CSF and total brain volume measured on the scanned data for SPIJN-MRF were in line with those obtained with SPM12 and FSL. The CoVs for white and gray matter volumes were distinctively higher for SPIJN-MRF than those measured with SPM12 and FSL. In conclusion, the use of SPIJN-MRF provides accurate and precise tissue relaxation parameter estimations taking into account intrinsic partial volume effects. It facilitates obtaining tissue fraction maps of prevalent tissues including myelin water which can be relevant for evaluating diseases affecting the white matter.

1. Introduction

Quantitative magnetic resonance imaging is getting increasingly more attention since several fast, multiparametric quantitative methods have emerged, e.g. MR-Fingerprinting (MRF) (Ma et al., 2013) and QRAPMASTER (Warntjes et al., 2008). The reduced scan-time of these acquisitions has facilitated their usefulness in research and clinical protocols (Nunez-Gonzalez et al., 2021; Chen et al., 2016; Badve et al., 2017; Ryu et al., 2020; Pirkl et al., 2021).

While these approaches can have a rich sensitivity to a wide range of tissue properties, the measurements are typically made voxel-wise, assuming a single tissue-type per voxel. However, partial volume effects are known to hinder this so-called single component approach (Giorgio and De Stefano, 2013; Ross, 2011; Heinen et al., 2016; de Bresser et al., 2011). Several methods were proposed facilitating multi-parameter estimates for a range of tissue components in a voxel. Examples of such multi-component techniques for MRF are modeling the signal with 3 *a priori* defined tissues (Ma et al., 2013), a Bayesian approach (McGivney et al., 2018; Deshmane et al., 2019), a reweighted-L_1-norm regularized algorithm (Tang et al., 2018), and a region-wise Greedy approximation method (Duarte et al., 2020). Following the principles of MRF, other techniques modeled bi-compartment voxels to distinguish between water and fat in cardiac MRF (Jaubert et al., 2020), to separate tissue from blood in arterial-spin-labeling MRF (Su et al., 2017) or estimated T_1-T_2 spectra per voxel (Kim et al., 2022). However these methods are limited by long computation times, a restricted number of pre-defined tissues within a voxel, and assume predominantly single

compartment voxels or concern very different types of multi-parameter acquisitions.

Another recently published method for coping with different tissue types within a voxel is the Sparsity Promoting Iterative Joint Non-negative least squares algorithm that was applied to MRF data (Nagtegaal et al., 2020) (SPIJN-MRF). This approach asserted joint sparsity of the number of tissue components in a region of interest, i.e. in a voxel as well as spatially. A priori no assumptions are made about the number of tissues and relaxation times while the method still proved faster than previously proposed techniques. As such it yields tissue parameters for each identified tissue component as well as tissue volume fraction maps. The SPIJN-MRF algorithm estimated brain tissue fraction maps from fully sampled MRF data with promising accuracy and precision (Nagtegaal et al., 2020). These maps particularly showed components representing myelin water, white matter (WM), gray matter (GM) and cerebrospinal fluid (CSF) components. To be able to distinguish myelin water is specially relevant in the diagnosis and evaluation of multiple sclerosis (MS), since it has been shown that patients have reduced myelin water content (Laule et al., 2008; Mackay et al., 1994; Laule et al., 2006; Kolind et al., 2015). Also, imaging the increasing myelin content of the developing brain has been done in several initial studies (Cencini et al., 2021; Chen et al., 2019).

Although the initial results with the SPIJN-MRF method were encouraging, an extensive study into the accuracy and precision of the method has not yet been performed. Additionally, it is unknown how the obtained brain tissue fraction maps relate to existing methods for tissue segmentations.

The aim of this work is to evaluate the accuracy and repeatability of the SPIJN-MRF parameter estimations from highly undersampled MRF acquisitions. The accuracy of the method will be assessed through estimation of the relaxation times and tissue fractions on simulated data from the BrainWeb numerical phantom environment, including a comparison to conventional techniques: the Functional Magnetic Resonance Imaging of the Brain Software Library (FSL) and the Statistical Parametric Mapping Software (SPM12). Furthermore, the repeatability will be assessed through the parameter estimates in eight weekly repeated scan sessions in 5 healthy volunteers. As in the simulations, tissue fraction maps will be compared to the SPM12 and FSL segmentations.

2. Methods

2.1. Simulations

Numerical simulations using the 20 BrainWeb phantoms (Aubert-Broche et al., 2006) were performed to test the accuracy and precision of the segmentations obtained with SPIJN-MRF and T_1-weighted based methods (FSL,SPM12). The BrainWeb phantoms were based on multiple high resolution conventional weighted scans from 20 different healthy subjects. Simulations were performed with resolution $1 \times 1 \times 5mm^3$. T_2 values were as defined in the BrainWeb database, but for white and gray matter T_1=930 ms and 1300ms were used instead of 500 ms and 830 ms as these are more realistic relaxation times for 3T (Körzdörfer et al., 2019; Buonincontri et al., 2019).

The MRF data was created by simulating a gradient-spoiled MRF sequence with a train of 1000 radiofrequency pulses as in (Jiang et al., 2015). This was done by performing extended phase graph signal generation (Weigel, 2015; Hennig, 1988) for each tissue after which a weighted combination of the signals based on the BrainWeb partial volume fractions yielded the MRF images. Subsequently, independent random complex Gaussian noise with standard deviation $\sigma = \max(abs(X))/100$ was added to each MRF image X_i, to yield the same noise level for all voxels and time points. No undersampling was performed in these simulations, as in (Nagtegaal et al., 2020).

The T_1-weighted images were also simulated by the BrainWeb simulator, using a spoiled FLASH sequence (TR=18ms, TE=10ms, FA=30

degrees), after which Rician noise was added with noise level parameter $\sigma = \max(abs(X))/100$.

The input tissue parameters and partial volume segmentations from the BrainWeb database served as ground truth values.

2.2. In vivo data acquisition

In vivo acquisitions were performed on a 3.0T GE MR750 MRI scanner (General Electric, Milwaukee, WI, USA). A Head, Neck and Spine array coil was used from which the 12 channels dedicated to the head were used for imaging.

Five healthy volunteers (3 females and 2 males, between 18–25 years) participated in this Institutional Review Board-approved study. All volunteers gave written informed consent to usage of their data prior to the first scan session.

MRF imaging was performed on the same day and time ($\pm$ 15 min) of the week for 8 consecutive weeks. As such the same gradient-spoiled MRF sequence as in the simulations was applied, varying the flip angle and the TR along a train of 1000 radiofrequency pulses (Jiang et al., 2015). The acquisition was performed with a FOV of 31 cm and slice thickness of 5 mm and slice gap of 1 mm (voxel size 1.2 mm x 1.2 mm x 5 mm). Total number of slices was 27, consisting of 256×256 voxels. The total scan time was 5 minutes and 54 seconds.

In each session, a READYBrain sequence (McMillan et al., 2022) was applied to align the MRF acquisitions to the anterior-posterior commissure (AC-PC) plane. READYBrain automatically detects the AC-PC plane for each subject and exploits this to plan the MRF with comparable imaging orientation across time and subjects.

Motion during 2D-MRF acquisitions is known to result in artifacts and errors in estimated T_1 and T_2 maps. Especially through-plane motion can lead to blurring and underestimation in T_2 (Mehta et al., 2018; Yu et al., 2018; Cruz et al., 2019; Kurzawski et al., 2022). Slices showing such through-plane motion artifacts were visually identified in single component T_1 and T_2 maps by notably deviating values compared to neighbouring slices before performing the multi-component analysis and excluded from further analysis unless explicitly stated otherwise. T_2 underestimation can also be caused by e.g. B_1^+ inhomogeneity. However, we assert that B_1^+ variation cannot cause abrupt changes in T_2 from slice to slice.

2.3. Image reconstruction

The acquired MRF data was reconstructed using an in-house implemented low-rank (LR) reconstruction algorithm in which the LR images were obtained while a compression matrix was iteratively updated. The spatial L_1 norm of the L_2 norm across the component images was applied for regularization purposes. A complete description of the used method can be found in Appendix I.

2.4. Single and multi-component parameter estimation

A dictionary was precomputed with the extended phase graph algorithm (Weigel, 2015; Hennig, 1988). This dictionary was created for T_1 values ranging from 100 ms to 3042 ms and T_2 values from 10 ms to 1030 ms, sampled with increasing step sizes by 5% (chosen as a compromise between dictionary size and resolution).

Synthetic T_1-weighted images were calculated based on the T_1, T_2 and M_0 maps estimated by single-component dictionary matching with the same settings as for the BrainWeb simulations. We chose to generate synthetic T_1-weighted images from the same data to have perfect spatial correspondence of the MRF and T_1-weighted data. As such differences in imaged volume were avoided. Based on the synthetic T_1-weighted images a brain mask was created using FSL-BET (Jenkinson et al., 2012).

Subsequently, the SPIJN-MRF algorithm (Nagtegaal et al., 2020) was applied to the MRF data, to obtain multi-component estimations for the

Table 1

Ranges used to categorize SPIJN-MRF tissue/material components (Bojorquez et al., 2017; Buonincontri et al., 2019; Dvorak et al., 2021; Körzdörfer et al., 2019; Mackay et al., 1994).

Name	T_1 range (ms)	T_2 range (ms)
White matter (without myelin water)	800–1050	50–100
Gray matter	1050–1500	50–100
CSF short T_2	2000–4000	9–300
CSF long T_2	2000–4000	300–2000
Myelin water	99–500	9–20
Veins and arteries	500–2000	200–1200

tissues present in the brain mask region. The SPIJN-MRF algorithm is based on the following optimization function:

$$\hat{C} = arg \min_{C \in \mathbb{R}_{\geq 0}^{N_A \times J}} ||X - DC||_F^2 + \lambda \sum_i^N ||C_i||_0,$$

Where X are the (compressed) MRF images with J voxels per time frame, D is the (compressed) dictionary with N_A atoms and C consists of N_A tissue fraction maps C_i of J voxels. The regularization parameter λ balances the data fidelity and joint sparsity regularization terms. Multi-component estimations were performed for all slices simultaneously. This yielded tissue parameters and magnetization fractions per voxel. Note that the number of tissues is not fixed a priori, but controlled through a sparseness constraint. A regularization value λ of 0.03 was used in the multi-component analysis. This regularization level was manually determined for one *in vivo* dataset and kept constant with all subsequent numerical and *in vivo* analyses.

2.5. SPM12 and FSL segmentations

The conventional methods were applied to the synthetic T_1-weighted images (created as described above). FSL-FAST (Jenkinson et al., 2012; Zhang et al., 2001) was applied after brain extraction (through FSL-BET) to obtain tissue segmentations while using default settings. SPM12 segmentation (SPM12, 2019; Ashburner and Friston, 2005) was also used with default settings, but the sampling distance was set to 1 instead of 3 to produce the most accurate segmentations (at the cost of consuming more time and memory resources). Tissue volumes in a voxel were calculated by multiplying obtained tissue probabilities in a voxel from SPM12 and FSL with the voxel size.

2.6. Atlas registration

To facilitate assessment of particular brain regions, all imaging data was aligned to the ICBM 152 Nonlinear atlases version 2009 (Fonov et al., 2011; Fonov et al., 2009). This alignment was based on the synthetic T_1-weighted images using the Diffeomorphic Anatomical Registration through Exponentiated Lie algebra (DARTEL) algorithm (Ashburner, 2007) as implemented in SPM12 (SPM12, 2019). Subsequently, the obtained deformations were applied to all SPIJN-MRF, SPM12 and FSL partial volume segmentations to achieve voxel-wise alignment to the atlas. All subsequent analyses focused on a common brain region, specifically: the region for which the mean intracranial volume fraction per voxel (WM+GM+CSF) was at least 75% with all segmentation methods.

3. Analysis

3.1. Tissue discrimination

From the SPIJN-MRF parameter estimations, different components were identified based on the relaxation times, see Table 1 (Mackay et al., 1994; Körzdörfer et al., 2019; Buonincontri et al., 2019; Bojorquez et al., 2017; Dvorak et al., 2021): myelin water, white matter (excluding

myelin water), gray matter, CSF and veins and arteries. CSF was partitioned into a short and long T_2 component after inspection of first results, as was observed in (Nagtegaal et al., 2020). Simultaneously, components with T_1 and T_2 relaxation times around 1s were identified, which we associated with *veins and arteries*. Total tissue volumes were calculated by summing the tissue fraction estimates multiplied by the voxel size (using an effective slice thickness of 6 mm to correct for slice gap).

3.2. Analysis of accuracy

The accuracy, i.e. systematic error, of the obtained SPIJN-MRF, SPM12 and FSL segmentations was evaluated using the simulated data. The agreement between estimated total white matter (including myelin water), gray matter and CSF volumes and the reference volumes was evaluated through Bland-Altman style plots. These showed the deviation from the reference as a function of reference value. Furthermore, the voxel-wise similarity between estimated partial volume and reference was assessed using the Fuzzy Tanimoto Coefficient (FTC) (Crum et al., 2006), which expresses the similarity of paired data as

$$FTC(A, B) = \frac{\sum_{i \in \Omega_{ROI}} \text{MIN}(A_i, B_i)}{\sum_{i \in \Omega_{ROI}} \text{MAX}(A_i, B_i)} \qquad \text{(Eq. 1)}$$

where A,B is a pair of tissue fraction maps of a complete volume, specific region or slice; subscript i represents a spatial index of the concerned voxels. The FTC is an adaptation of the Jaccard index or Tanimoto coefficient for non-binary segmentations.

3.3. Analysis of repeatability

The repeatability of the SPIJN-MRF method was determined for the *tissue parameter* estimations and *partial volume segmentations* on the *in vivo* imaging data.

First, the mean and standard deviation of the SPIJN-MRF relaxation times were calculated per subject and tissue over the eight different time points. Subsequently, the repeatability was evaluated based on the range of standard deviations across the subjects per tissue.

Second, the repeatability of tissue volume estimation of the SPIJN-MRF and conventional methods over the time points was evaluated voxel-wise, in different brain regions and for the entire brain per tissue. In each case the mean value and corresponding standard deviation was determined per subject across the time points. The repeatability was quantified using the Coefficients of Variation (CoV = $\frac{\sigma}{\mu}$, where σ is the standard deviation and μ is the mean of the tissue volume over the 8 scan sessions) and the Combined Fuzzy Tanimoto Coefficient (CFTC) (Crum et al., 2006) for each subject and tissue

$$CFTC(A) = \frac{\sum_{k=1}^{\#days-1} \sum_{j=k+1}^{\#days} \sum_{i \in \Omega_{ROI}} MIN(A_{ki}, A_{ji})}{\sum_{k=1}^{\#days-1} \sum_{j=k+1}^{\#days} \sum_{i \in \Omega_{ROI}} MAX(A_{ki}, A_{ji})}, \qquad \text{(Eq. 2)}$$

where A_{ki} denotes the volume fraction of voxel i at day k for a subject and tissue of interest.

3.4. Comparison with conventional methods

Initially, comparison of the methods was performed by visual assessment of the segmentation maps. Subsequently, estimated total tissue volumes for the entire brain and per region were compared across the methods. While doing so, the volume fractions obtained with SPIJN-MRF for white matter and myelin water were summed into a single white matter tissue. Similarly, the SPIJN-MRF CSF fractions of long and short T_2 times were summed to yield the total CSF partial volumes. CoVs and CFTCs for total brain tissue volumes were calculated including and excluding the slices with motion artifacts to evaluate the effect of these artifacts on the repeatability.
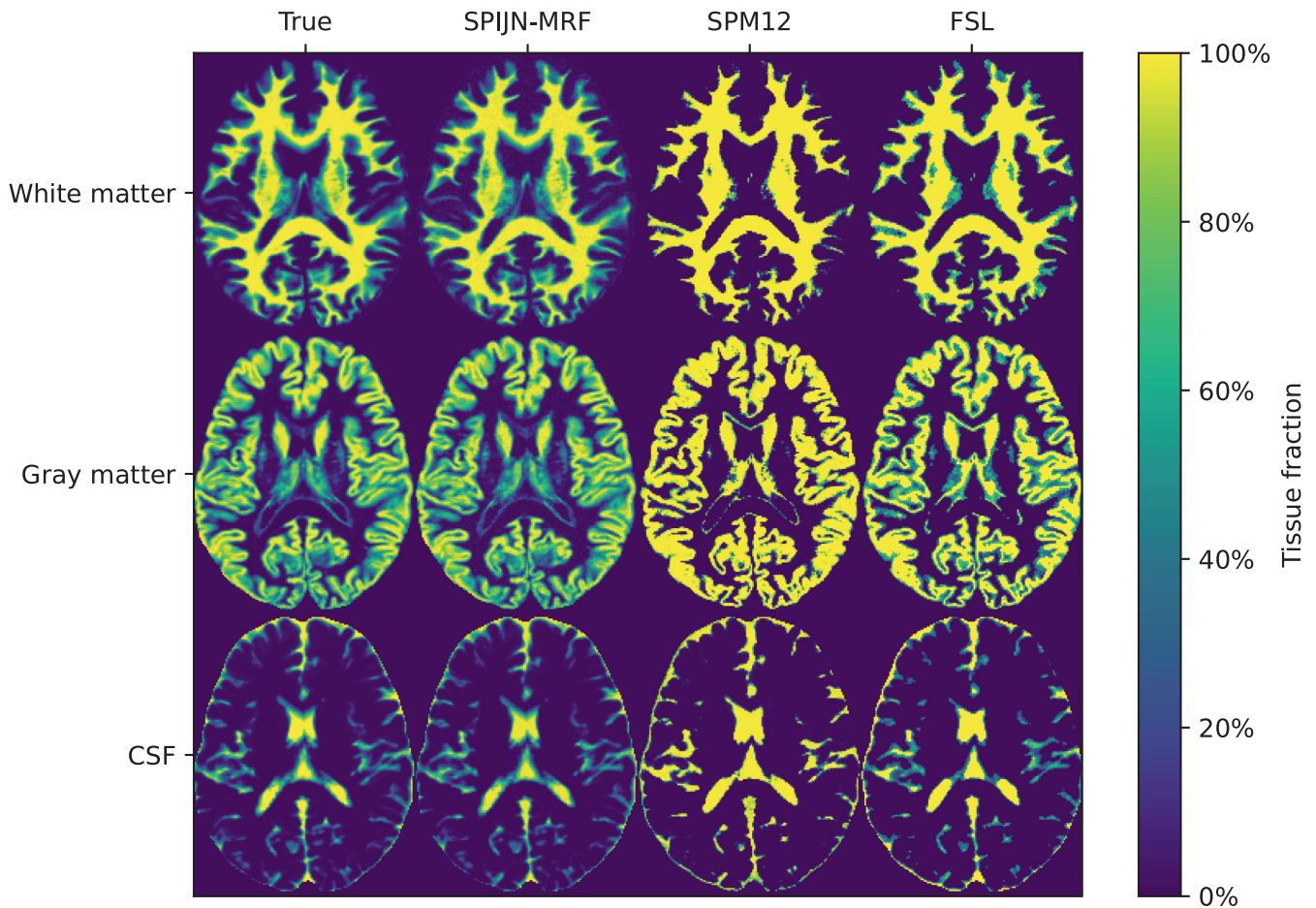
Fig. 1. Example of partial volume segmentations obtained with multi-component MRF, SPM12 and FSL in simulations based on the central slice of a BrainWeb phantom (first column).

4. Results

4.1. Simulations

SPIJN-MRF yielded exact estimates of underlying T_1 and T_2 tissue parameters in all 20 datasets. Fig. 1 shows representative partial volume segmentations obtained with SPIJN-MRF, SPM12 and FSL. Observe that the SPIJN-MRF images closely resemble the ground truth with soft transitions between tissue and background, while these transitions are sharper in the SPM12 and FSL segmentations.

Fig. 2 shows Bland-Altman style plots, for each subject, method and the three tissues of interest, with the deviation from the true total tissue volume (vertically) as a function of the true value (horizontally). The mean deviations from the true value are indicated by solid lines. Limits of agreement are delineated by the light blue regions.

It can be observed that SPIJN-MRF and FSL showed little bias (defined as only a small deviation from the true value), whereas marked bias was found with SPM12. All three methods had the lowest bias in gray matter compared to the other tissues (max 3.3 cm^3 for SPM12). SPM12 had the largest bias for white matter (mean deviation -78.4 cm^3).

The limits of agreements between the estimated volumes and the reference values were smaller for SPIJN-MRF than for SPM12 and FSL, indicating that the differences between SPIJN-MRF estimations and the true values vary less than for SPM12 and FSL. SPM12 had the largest spread in the limits of agreements, which indicates a lower precision.

Fig. 3 shows the distribution of FTCs obtained with SPIJN-MRF, SPM12 and FSL. In all the tissues, the segmentations performed by SPIJN-MRF were the most similar to the true segmentations, with FTCs around 0.97. SPM12 and FSL had lower FTCs: between 0.6 and 0.7 for white and gray matter and between 0.5 and 0.6 for CSF, respectively. Segmentations made with FSL had slightly higher FTCs than segmentations with SPM12. FTCs varied across slices, following a similar trend as the total amount of tissue per slice (see Supplementary Fig. S1). A fixed SNR level (100) was used in the shown results, in additional experiments different noise levels led to similar findings as shown in Supplementary Figs. S2–S4.

4.2. In vivo data analyses

A total of 10 MRF acquisitions (out of 40) were affected by motion artifacts in one or more slices. It concerned 3% of the total number of slices. Computation times were approximately 50 minutes for SPIJN-MRF estimations on a standard desktop pc (Intel i7-8650U CPU 1.9GHz, 8GB RAM).

4.2.1. Tissue discrimination

Fig. 4 shows all components resulting from the MRF data of a single acquisition across several slices from one representative subject. The leftmost column shows the T_1 and T_2 values for each of 9 identified components while the images depict corresponding estimated tissue fractions.
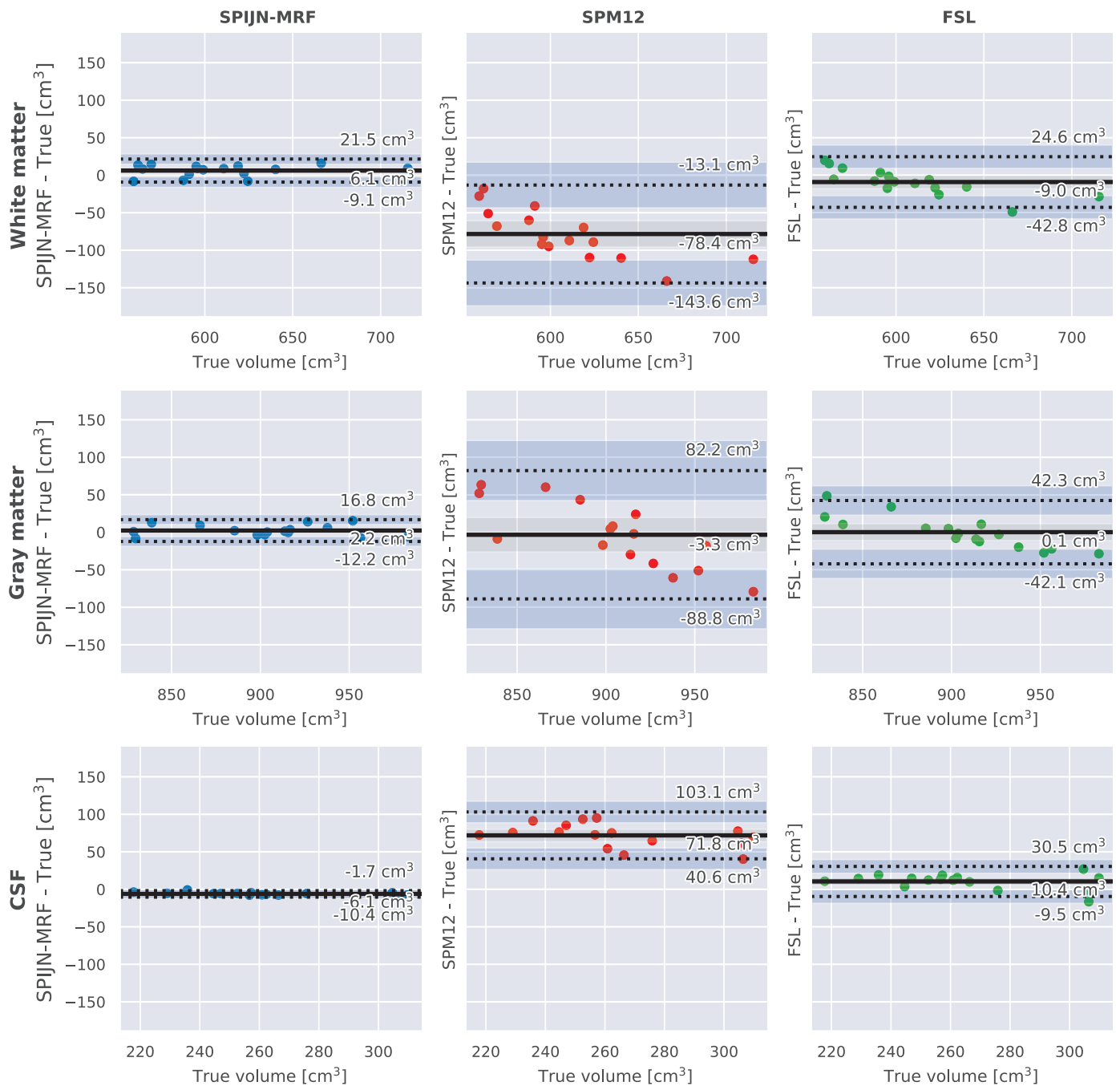
Fig. 2. Bland-Altman style plots showing the deviation (vertically) from the true volume in the 20 BrainWeb phantom volumes obtained with the SPIJN-MRF (left), SPM12 (middle), and FSL (right) methods. The solid lines indicate the mean deviation in each plot (i.e. the bias), the exact value of which is indicated next to each line. Dotted lines reflect the limits of agreement (1.96 times the standard deviation of the bias). Shadowed areas in gray and blue delineate the 95% confidence interval of the mean and the limits of agreement respectively.

In Fig. 5, the main component maps and standard deviation (std) maps (after registration) obtained after grouping as per Table 1 for a central slice from the same subject are depicted for each acquisition day. Observe that there are minimal differences over time (as reflected in the std maps in the right column). Global intensity variations can be observed in the myelin water map (in particular concerning scans 5 and 6 seem to yield higher tissue fractions). However, for the other tissues the variability is similar across the brain.

Table 2 collates the means and standard deviations of T_1 and T_2 relaxation times across all subjects and scans per tissue as well as the mean intra-subject standard deviations per tissue. On average 8.3 com-

ponents were identified over all acquisitions (26 times 8 components, 13 times 9 and 1 time 10). No components were outside the predefined ranges (Table 1). The mean intrasubject standard deviations of *myelin water* and *veins and arteries* for T_1 estimation and of short CSF for T_2 estimation was larger than 10% percent of the reported mean value. For all other tissues the intrasubject standard deviations of T_1 and T_2 relaxation times showed small variation. After changing the dictionary ranges the observed clipping to the dictionary boundaries appeared persistent and visually did not appear to affect the estimated partial volume maps. Supplementary Fig. S5 shows scatter plots of the estimated T_1 and T_2 values across subjects and scans.
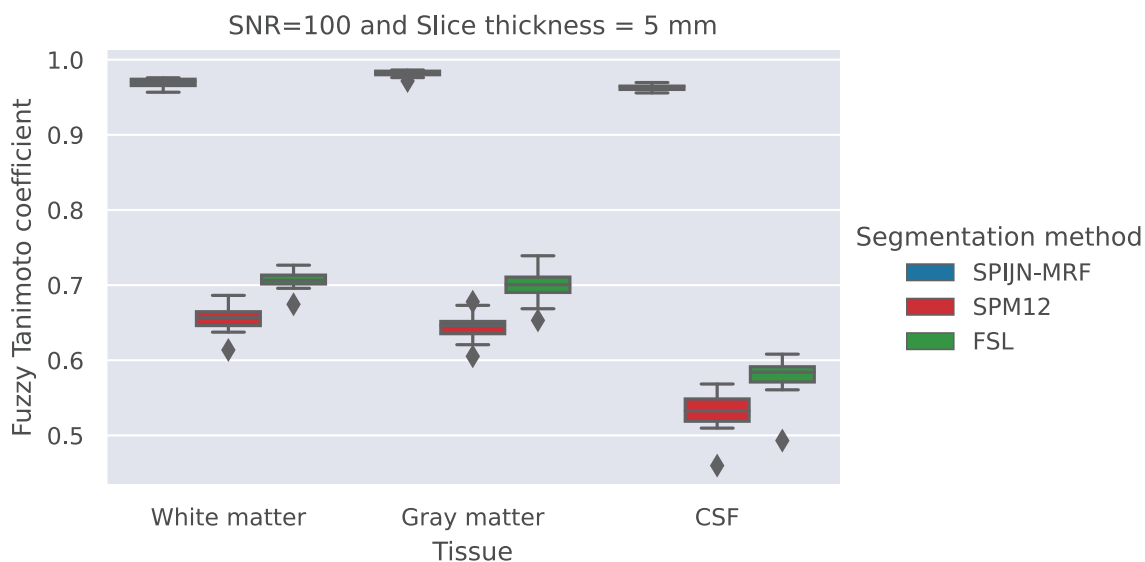
Fig. 3. Box plots showing distributions of the Fuzzy Tanimoto Coefficient (FTC) for white matter (left), gray matter (middle), and CSF (right) comparing the 20 BrainWeb phantoms and the tissue segmentations using SPIJN-MRF(blue), SPM12 (red), and FSL (green).
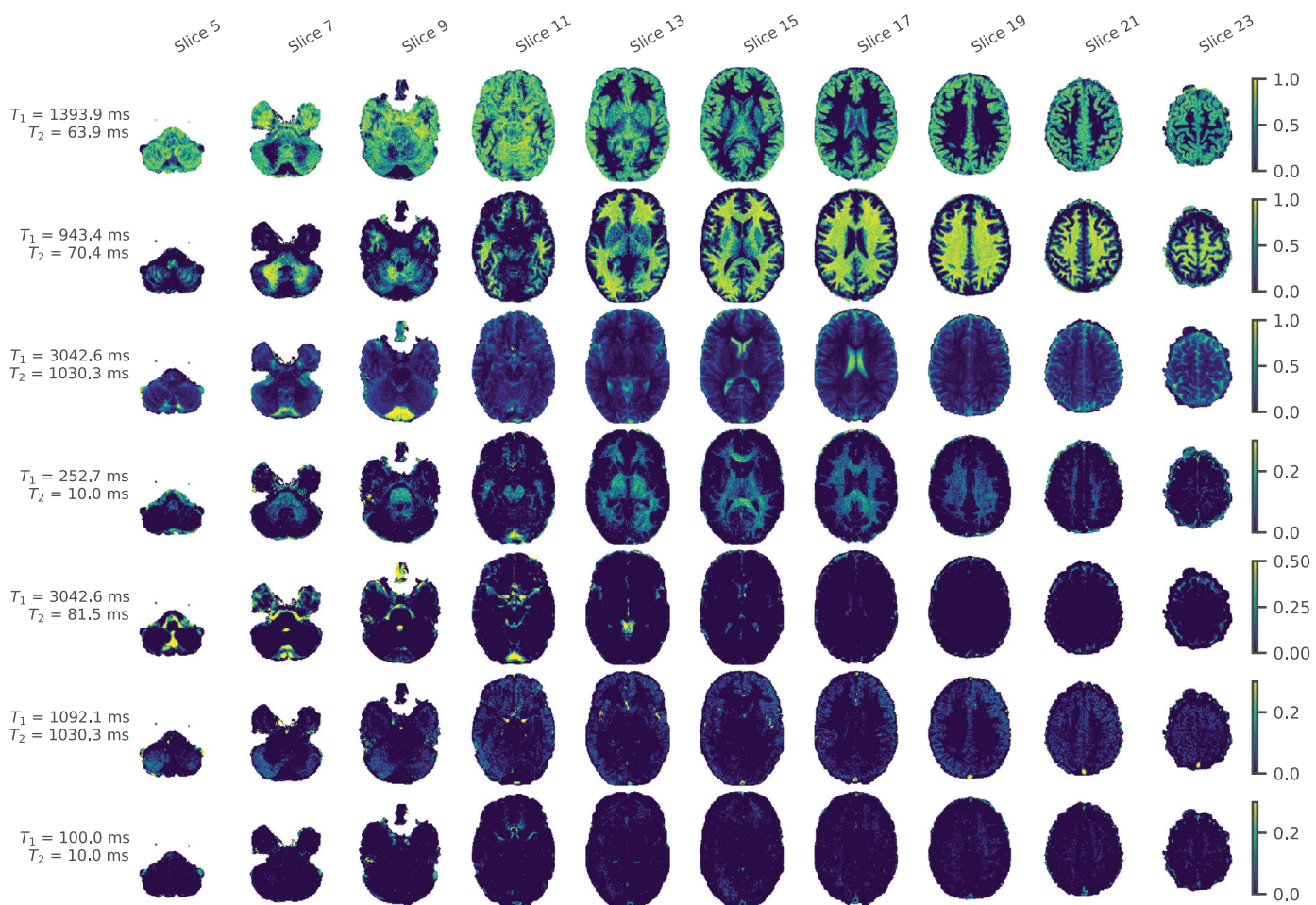
Fig. 4. Multi-component tissue fraction maps for one MRF dataset of a single subject. Obtained T_1 and T_2 relaxation times are shown in the left column. Note that the component maps are only estimated inside the brain mask. For illustration purposes only the ten central odd slices are shown instead of the total 28 slices and components with a relative volume fraction of less than 1% were not shown.
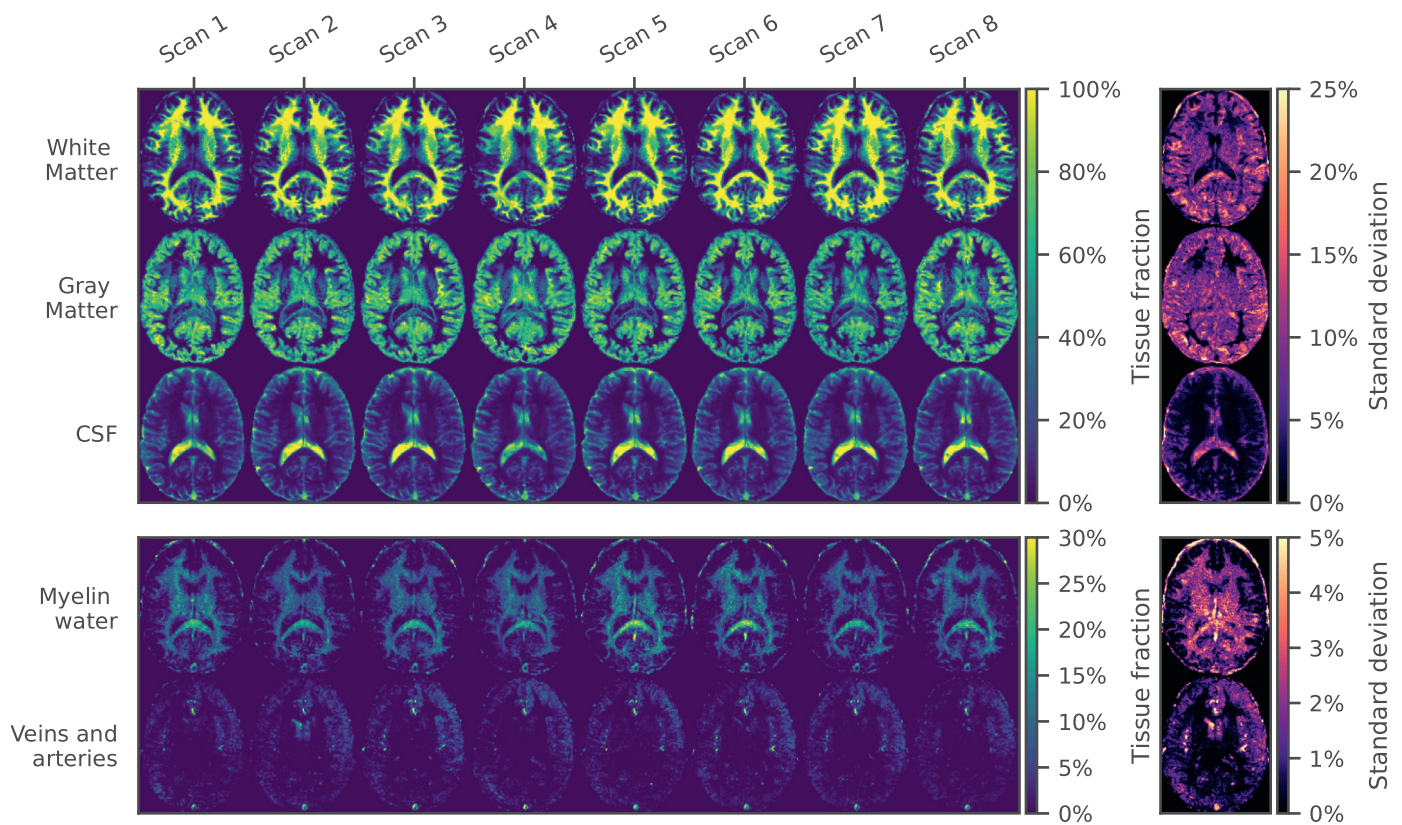
Fig. 5. SPIJN-MRF maps across days and tissue types are for a central slice for one subject after grouping based on relaxation time. Note that the lower two rows use a different color range for illustration purposes. Standard deviation maps are shown in the column on the right.

Table 2

Means and corresponding standard deviations (std) of estimated T_1 and T_2 relaxation times across all 5 subjects and 8 repeated scans per tissue as well as the means of 5 intrasubject standard deviations per tissue. *T_1 or T_2 values are the minimum/maximum value represented in the dictionary, which also occured with extended boundaries.

Tissue	T_1 (ms)		T_2 (ms)	
	Mean ± Std across all subjects and scans	Mean intra-subject standard deviation	Mean ± Std across all subjects and scans	Mean intra-subject standard deviation
White matter excluding myelin water	943.4 ± 0.0	0.0	69.2 ± 1.2	2.5
Gray matter	1383.9 ± 10.8	17.7	62.3 ± 1.2	1.7
CSF longer T_2	3042.6 ± 0.0*	0.0	1030.3 ± 0.0*	0.0
CSF shorter T_2	3042.6 ± 0.0*	0.0	149.3 ± 9.4	18.3
Myelin water	230.7 ± 20.1	34.0	10.0 ± 0.0*	0.0
Veins and arteries	876.2 ± 93.9	106.7	1030.3 ± 0.0*	0.0

Table 3

CoVs of the estimated total myelin water volume, white matter volume (including myelin water), gray matter volume, CSF volume and total brain volume. The last column reports the mean of the CoVs over all subjects.

| Tissue	Subject					Mean
	A	B	C	D	E	
Myelin water (MW)	13.7%	13.3%	4.4%	13.3%	7.6%	10.5%
White matter (including MW)	3.8%	6.4%	7.0%	4.7%	8.2%	6.0%
Gray matter	3.4%	5.5%	8.7%	3.7%	6.6%	5.6%
CSF	6.4%	6.5%	6.4%	2.1%	1.7%	4.6%
Brain volume	1.0%	1.7%	1.8%	0.5%	0.7%	1.1%

4.2.2. Repeatability

Table 3 presents the CoVs of the total volume estimates of myelin water, white matter (including myelin water), gray matter, CSF and the total brain volume (WM + GM) across subjects. Total brain volume showed minor variation (mean CoV = 1.1 %); the volume estimates of CSF, GM and WM (including MW) were slightly more variable, with mean CoV

of 4.6%, 5.6% and 6.0%, respectively, while MW by itself had higher mean CoV (10.5%).

4.2.3. Comparison with brain volume measurement methods

Fig. 6 illustrates that the SPIJN-MRF tissue maps from the *in vivo* data contained more gradual transitions between brain tissues than the con-
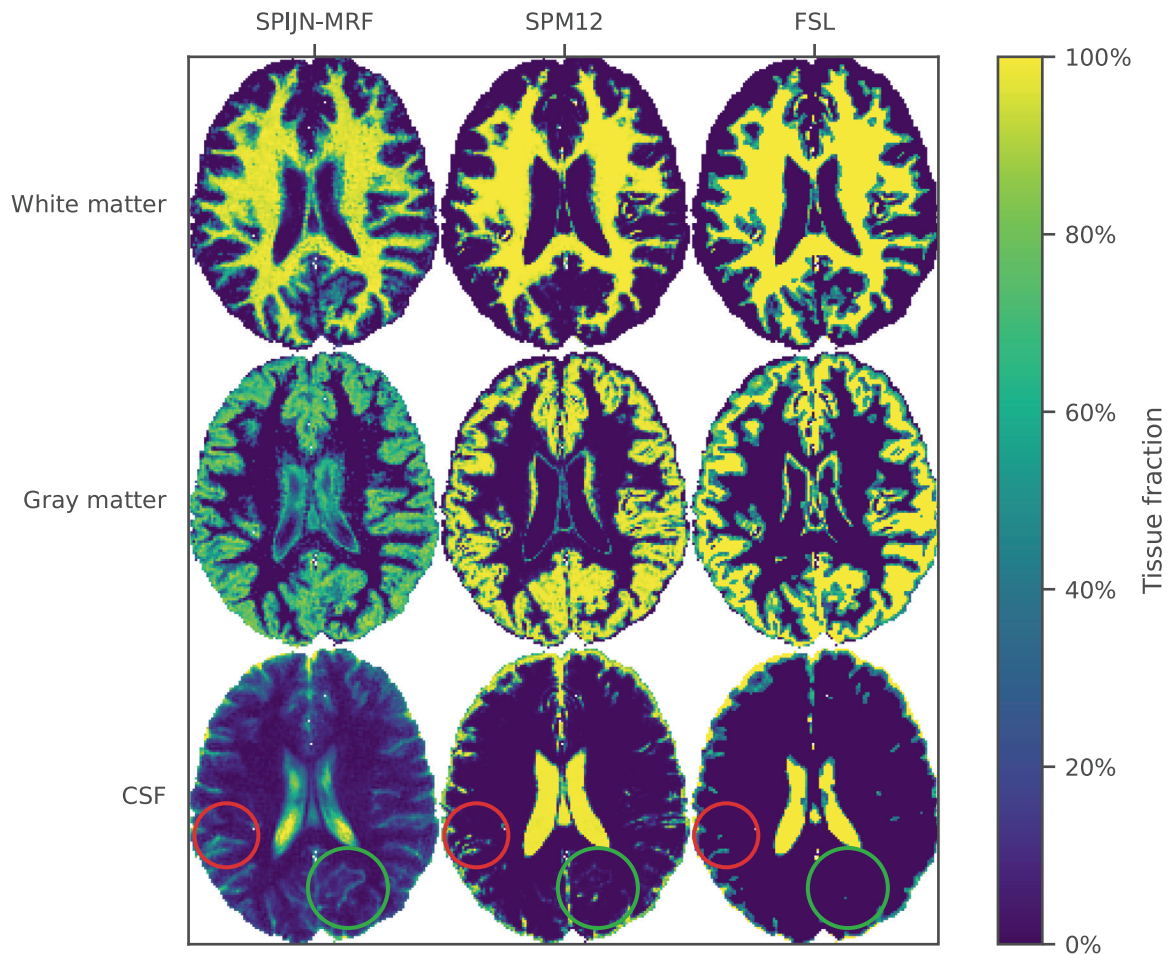
Fig. 6. A representative slice showing the white matter (top), gray matter (middle) and CSF (bottom) fraction maps obtained using SPIJN-MRF (left), SPM12 (middle), and FSL (right) for one single acquisition of one subject (subject B, day 5). Red and green circles point out notable differences in CSF between methods.

ventional methods, similar to simulated data. For instance, the SPIJN-MRF CSF map shows small details not observed in the other maps (green circle) whereas parts are more confined in the SPM12 and FSL segmentations (red circle). Furthermore, the GM SPIJN-MRF component was almost always identified as a mixture of GM and CSF or WM components (maximal GM fraction around 90%). This highlights the ability of SPIJN-MRF to approximate brain tissue content of partial volume voxels.

The distributions of total volumes for each subject with SPIJN-MRF, SPM12 and FSL are collated in Fig. 7. It can be observed that SPM12 estimates are lower in white matter than FSL estimates, and consequently, the opposite is noticeable for gray matter and CSF as the sum of tissue percentages is 100% by definition. In general, the estimated volumes with SPIJN-MRF appear between the estimated volumes of SPM12 and FSL. Furthermore, the SPIJN-MRF volume distributions show a larger spread than those of SPM12 and FSL.

In Fig. 8, the estimated relative volumes per anatomical region for each tissue, method and subject are summarized (see Supplementary Fig. S6 for absolute volumes per region). In general, the three methods had relatively similar relative volumes per region. However, for the cerebellum and for the deep gray matter FSL gave higher white matter volume than SPIJN-MRF and SPM12 in all subjects. As a consequence, FSL yielded lower gray matter volumes.

Fig. 9 shows CFTCs (upper row) and CoVs (lower row) for the motion-artifact-free data and the full dataset across the subjects and the tissues.

The SPM12 yielded slightly higher CFTC than SPIJN-MRF in white and gray matter in all subjects. SPIJN-MRF gave higher CFTCs compared to both SPM12 and FSL in CSF, which was observed consistently across slices (see Supplementary Fig. S7). Also, the CoVs of SPM12 and FSL were distinctly lower than those of SPIJN-MRF for white and gray matter, whereas differences were smaller for CSF and total brain volume.

The CoVs for SPIJN-MRF were lower using the data without motion artifacts than with all data in all tissues but one in subjects C and D, and E. The only exception was in subject E, in which the white matter score was barely affected.

We did not observe a particular trend in the CFTCs nor in the CoVs of the motion-artifact-free data related to anatomical region nor any specific differences between left/right brain regions (see Supplementary Fig. S8).

5. Discussion

This paper aimed at evaluating the accuracy and repeatability of the joint sparsity based SPIJN-MRF estimations (Nagtegaal et al., 2020). The results show that it yields accurate brain tissue voxel fraction estimation in simulated data (mean systematic errors between 2cm^3 and 6cm^3 and Fuzzy Tanimoto Coefficient above 0.95) and gives good repeatability in *in vivo* data (Fuzzy Tanimoto Coefficient above 0.7 and mean (across subjects) CoVs between 5.7% and 6.1%).

In simulations, we observed that the white matter, gray matter and CSF fraction maps obtained with SPIJN-MRF had smaller systematic er-
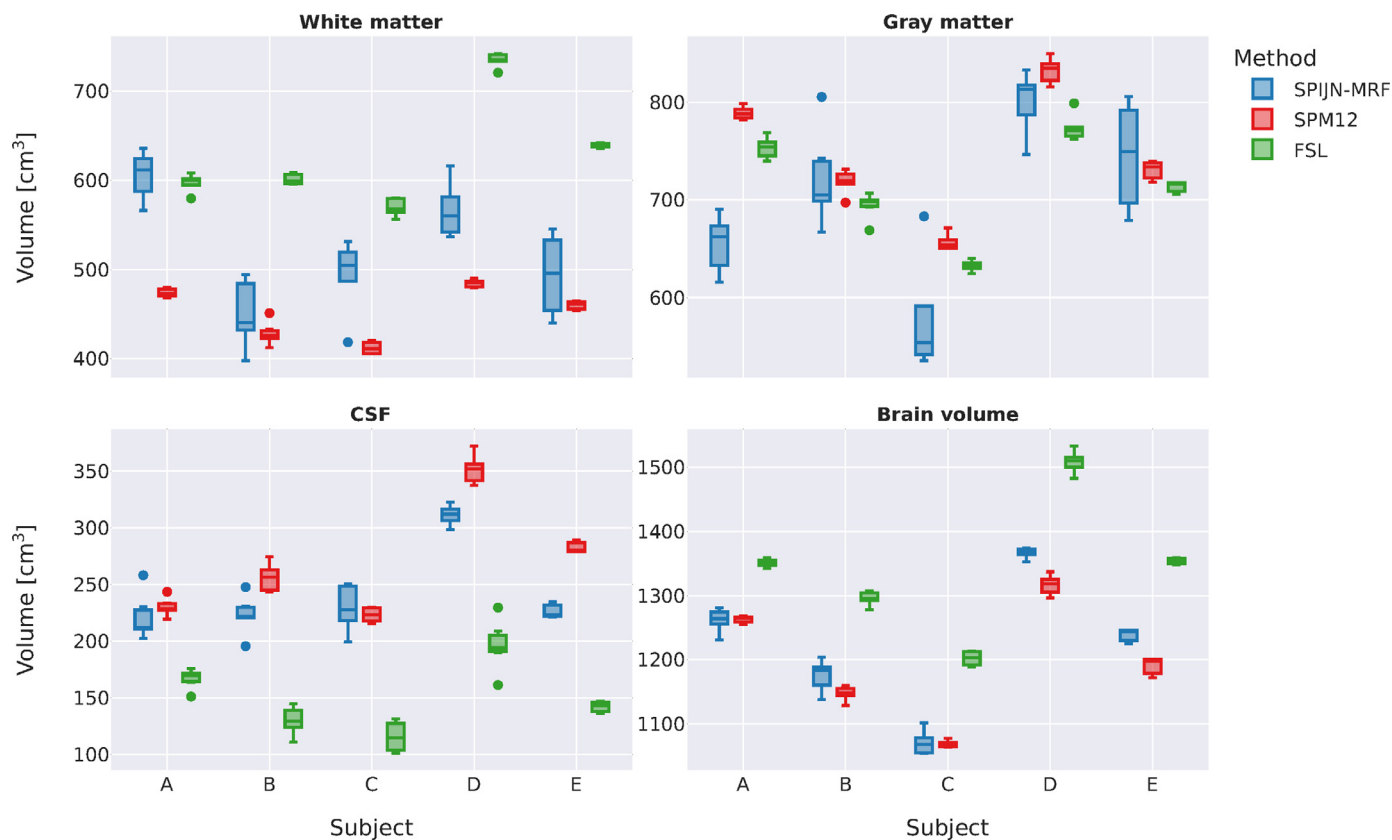
Fig. 7. Box plots showing for each subject the total volume of the white matter (top-left), the gray matter (top-right), the CSF (bottom-left), and the total brain (bottom-right) estimated using SPIJN-MRF (blue), SPM12 (red) and FSL (green).

rors than those obtained with SPM12 and FSL in both total volume estimation as voxel-wise similarity.

The T_1 and T_2 values obtained by SPIJN-MRF from the *in vivo* data for each component were very stable for all the acquisitions and in the range of previous quantitative studies (Mackay et al., 1994; Bojorquez et al., 2017; Stanisz et al., 2005; Alonso-Ortiz et al., 2015; Bouhrara and Spencer, 2017). The observed standard deviation of zero for WM derives from the dictionary resolution (which is 5% for T_1 values) and resulted from repeated selection of the same dictionary atom. Previous studies have reported variations in T_1 below 5% (Nunez-Gonzalez et al., 2021; Buonincontri et al., 2019). Unexpectedly and contrary to the single-component estimations, we found that the T_2 value from the white matter component was slightly longer than the T_2 value found for the gray matter (see Table 2). This can be partly due to the attribution of myelin water (having a very short T_2 time) to a separate component independently of white matter, whereas values reported in the literature for white matter commonly include myelin water In effect, this will lead to longer relaxation values for the 'pure' white matter component, merely as a shorter time component is left out. Previously, a thorough study of the T_2 distributions in the brain indeed demonstrated that T_2 distributions are affected by properties of the spaces between myelin sheaths (Whittall et al., 1997).

Furthermore, CSF was consistently represented by two different components, one with longer T_2 (around 1 s) and one with shorter T_2 (around 150 ms). This separation could be caused by the choroid plexus within the ventricles or by flow effects. The identification of the *veins and arteries* component as shown in Fig. 5 was not observed before in multi-component relaxometry to our knowledge. This component had high T_1 and T_2 times (both around 1s) and consistently appeared in all subjects and scans. Further research into physiological understanding of this fluid-like component would be an interesting direction for future work.

Estimated T_1 relaxation times showed a very high repeatability, but for some components the maximum T_1 value of the dictionary was selected. The use of a maximum T_1 value of 6s instead of 3s did not affect this biasing effect (data not shown here) and was therefore not used any further. For better estimation of T_1 relaxation times in CSF a different MRF sequence and dictionary range would probably be required to improve discrimination between long T_1 components.

The consistent estimation of a separate myelin water fraction (MWF) map with the SPIJN-MRF approach could be useful, e.g. for assessment of multiple sclerosis as well as other white matter diseases (Mackay et al., 1994). A comparison to other MWF estimation methods (Piredda et al., 2021) would be needed to further validate our technique, although differences between methods are known (Alonso-Ortiz et al., 2018; Dvorak et al., 2021).

A SPIJN regularization of 0.03 was used in the analysis resulting in reproducible estimates. We observed that changes from 0.025 to 0.035 led to only small changes in MW and veins/arteries component relaxation times and volume fractions, while WM/GM/CSF were less affected by the regularization. The required regularization will be affected by the SNR level and might therefore require adaptation for different scanners, sequences, or reconstructions.

The study on the repeatability of the SPIJN-MRF yielded CoVs < 10% for the total white matter volume (including myelin water), the gray matter volume and the CSF volume for all subjects. This variation of the estimated volumes with the SPIJN-MRF is similar to the variation found previously with commonly accepted methods, such as SPM12 and FSL (Tudorascu et al., 2016; Klauschen et al., 2009). The estimation of the myelin water volume showed more variation (average CoV = 10%) than other tissues. The repeatability was similar across the whole brain, even though we applied a rather large slice thickness.This signifies the robustness of the method also in regions with large susceptibility vari-
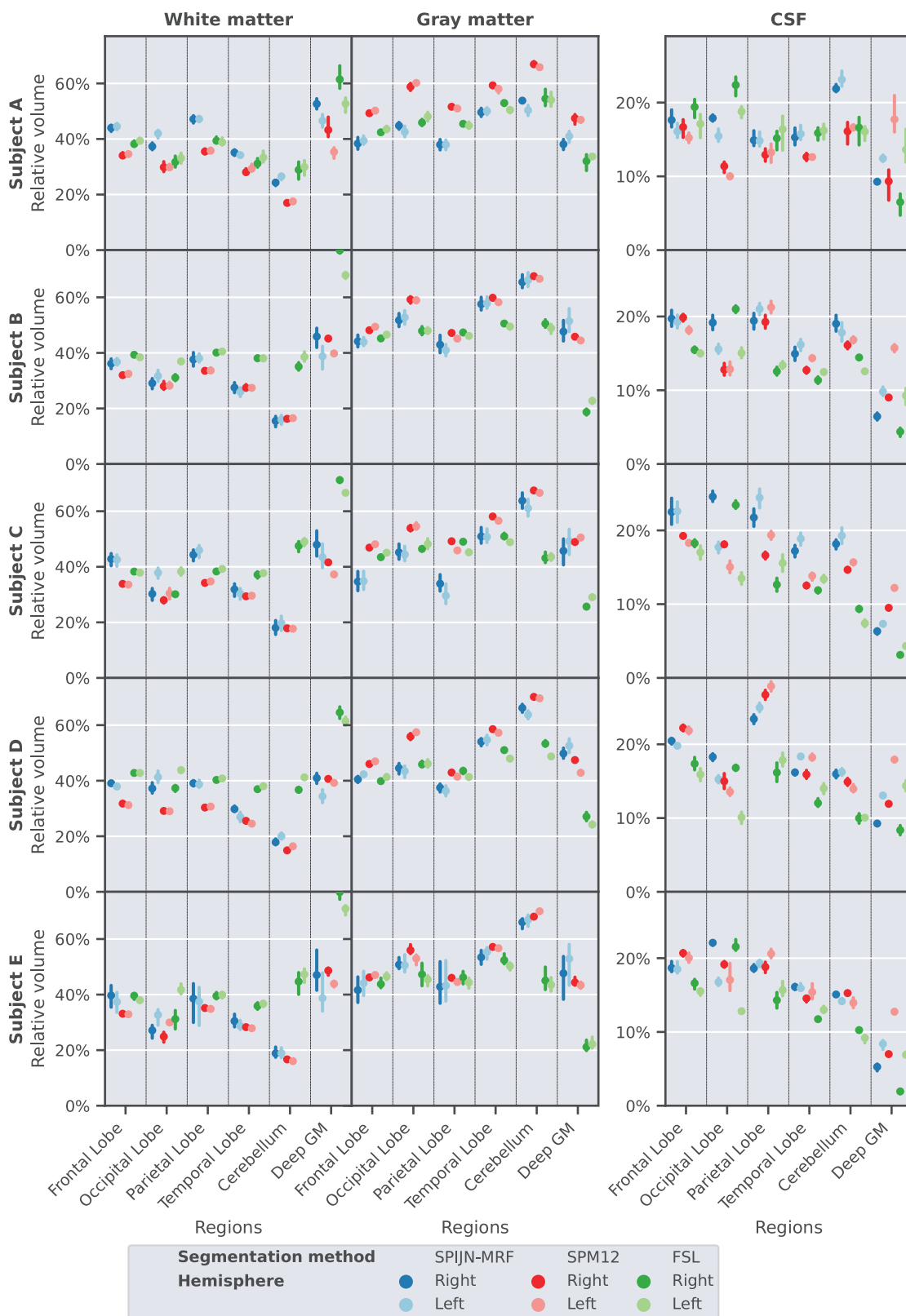
Fig. 8. Mean relative volume for each subject over time (dots) and associated standard deviation (vertical lines) for different anatomical regions of the white matter (left), the gray matter (middle), the CSF (right) estimated using SPIJN-MRF (blue), SPM12 (red) and FSL (green).
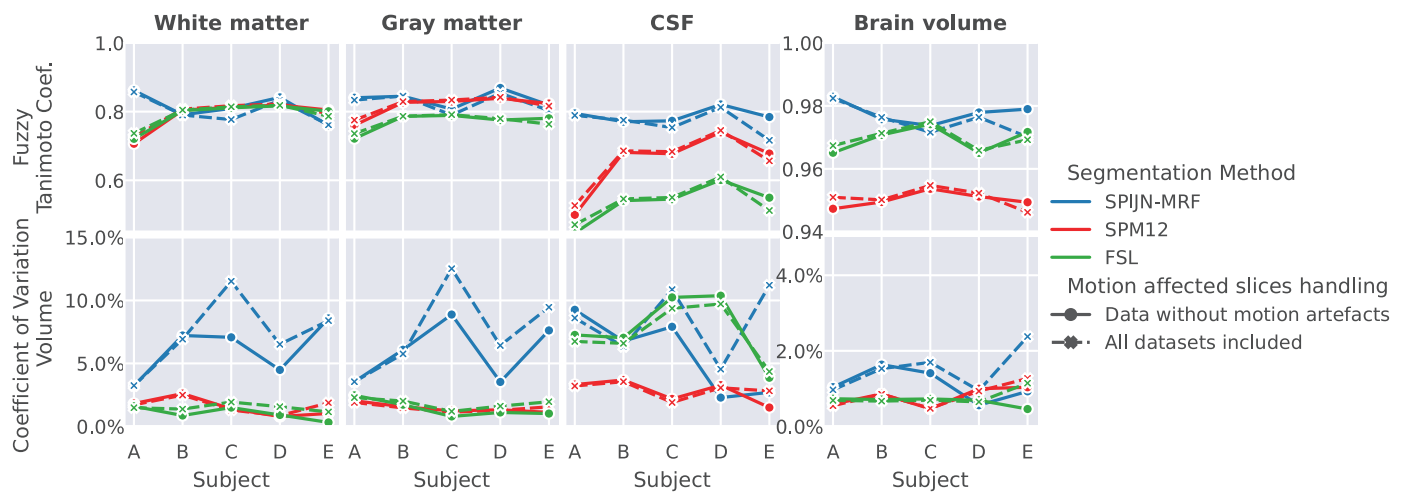
Fig. 9. Combined Fuzzy Tanimoto Coefficient and CoV of estimated total volumes for each subject for white matter (including myelin), gray matter, CSF and total brain (white matter plus gray matter) obtained with SPIJN-MRF (blue), SPM12 (red), and FSL (green). Results from the data without motion artifacts are depicted using circles and solid lines, results obtained using all data are depicted with squares and dashed lines.

ations such as in areas with air (frontal part) or areas with more iron (deep gray matter).

The closer resemblance of the SPIJN-MRF maps to the reference in the simulations was reflected in higher FTC values with smaller standard deviations compared to the conventional methods. Especially in the CSF maps (both in simulation and *in vivo*), more details of the anatomy were visible with the SPIJN-MRF method than with SPM12 and FSL. These results could indicate that SPIJN-MRF improves measuring partial volume properties of smaller brain structures. Furthermore, compared to SPM12 and FSL it may provide new information, such as the myelin water fraction. To validate the high accuracy in simulations, further investigation into the *in vivo* accuracy should be performed. Currently we considered this outside the scope of our *in vivo* study, which mainly focused on the repeatability of SPIJN-MRF. Post-hoc, we performed as a preliminary approach to an accuracy evaluation, a small follow-up study one of the subjects that was rescaneed four times indicating similar performance in volume estimation of SPIJN-MRF compared to conventional SPM12 and FSL segmentation using conventional, high resolution T_1-weighted acquisitions (see Supplementary Fig. S9). Furthermore, FSL and SPM12 recommend using T1w-MPRAGE for segmentation, while our simulated images were created based on a spoiled FLASH sequence as was used for the BrainWeb simulations. Although the resulting images have a very similar contrast (see Fig. S10), the set of parameters for the synthetic T_1-weighted images can be optimized further and the reported accuracy might be slightly affected by the generated contrast.

SPM12 uses a probability atlas with anatomical information to segment the brain tissues, which could enhance the repeatability of results but potentially also introduces a bias. FSL uses a hidden Markov random field model and an expectation-maximization algorithm to obtain robust results with improved denoising, but this might lead to removing small brain structures. Instead, the joint sparsity multi-component MRF model does not incorporate explicit *spatial* regularization or anatomical a priori knowledge.

Differences in estimated brain tissue volumes between SPM12 and FSL were already previously reported (Tudorascu et al., 2016). Our estimated volumes for FSL are higher in white and gray matter and lower in CSF compared to SPM12 with the simulated data just as in Klauschen et al. (2009). Contrary to the simulated data, the estimated total brain volumes for the *in vivo* data by SPIJN-MRF are closer to the estimated volumes from SPM12 than those from FSL. Also, the relative volume per region calculated by SPIJN-MRF is closer to the relative volume calculated by SPM12 than FSL for the *in vivo* data. This could be caused by intrinsic differences between the T_1-weighted brainweb im-

ages (used in the simulations) and the MRF based T_1-weighted images (used in the *in vivo* experiments). The differences in the contrast could result in slightly different classification of the voxels and affect the local partial volume estimates.

In contrast to the simulations, the CoVs of SPIJN-MRF for *in vivo* data reflected higher variability than those of SPM12 and FSL for almost all subjects and tissues. The low variability of SPM12 and FSL, also in comparison with previous studies (Tudorascu et al., 2016; Klauschen et al., 2009), could be due to the use of synthetic images. This is because the quantitative parameters (M_0, T_1 and T_2) from MRF were highly repeatable, differing only between 0 and 2% amongst all the acquisitions. As a consequence the resulting synthetic T_1-weighted images are also highly similar. This likely biases the repeatability of the SPM12 and FSL segmentations. We chose to create synthetic T_1-weighted images in order to have perfect spatial correspondence of the data. As such differences in imaged volume were avoided.

SPM12 and FSL demonstrated to be slightly more robust against motion artifacts than SPIJN-MRF, resulting in minimal differences in CoV and FTC when using data without and with motion artifacts. Although motion effects were observed in a relatively small number of slices, it did affect the volume estimates. Simultaneously, however, estimated T_1 and T_2 relaxation times were not affected by motion affected slices. Nevertheless, our results show that efforts to minimize the impact of subject-motion in the MRF data may enhance in particular the repeatability, e.g. by applying motion-correction (Cruz et al., 2019) or 3D-acquisitions with possible use of navigators (Johnson et al., 2011) or self-navigations (Kurzawski et al., 2022).

A limitation of this work is that the evaluation of accuracy was mostly done on simulated data (see Figs. 2, 3 and Supplementary Fig. S9). Further validation of segmentation accuracy could be performed, for example by assessment of the segmentations through expert neuro-radiologists. Future work could also take into account other potentially relevant aspects in the simulations, such as: reconstructions from under-sampled data, modeling of B_0 or B_1^+ inhomogeneities, representation of the presence of myelin water or inclusion of other biological phenomena such as magnetization transfer or flow.

Another limitation could be that we did not include B_1^+ field inhomogeneity as a parameter in our SPIJN-MRF estimation. B_1^+ inhomogeneity might affect the SPIJN-MRF parameter estimation and especially MWF estimation. However, we did not observe particular spatial variations in the obtained fraction maps that appear to resemble smoothly varying B_1^+ inhomogeneities. Further research (including an acquired B_1^+ map) would be needed to explicitly study the effect of B_1^+ and to

analyze the potential benefits of accounting for B_1^+ variation in the estimation of the tissue fraction maps.

Furthermore, optimizing the MRF sequence for multi-component MRF estimations (Heesterbeek et al., 2021) to make it more sensitive to myelin water or to improve the distinction between gray and white matter could lead to further improvement of estimations, reduced scan times or the possibility to use a reduced slice-thickness. However, we consider the implementation of such optimization beyond the scope of our current paper.

6. Conclusion

We studied the accuracy and repeatability of the SPIJN-MRF method in simulations and *in vivo* brain MRI scans. SPIJN-MRF showed more accuracy and higher repeatability in simulated data than conventional methods (SPM12 and FSL). In the *in vivo* data, SPIJN-MRF consistently identified the same brain tissue components and gave highly repeatable relaxation times related to these tissues. SPIJN-MRF partial volume maps showed small details, also in CSF. The repeatability of the estimated brain tissue volumes of SPIJN-MRF was somewhat lower compared to SPM12 and FSL, possibly due to simulation bias . A further advantage of using SPIJN-MRF is the additional simultaneous estimation of MWF maps, which is not obtainable with single compartment-based methods.

Data and code availability statement

In-vivo reconstructed data is publicly available at 10.5281/zenodo.5576039.

The code for the SPIJN-MRF algorithm was previously published (10.1002/mrm.27947) and available at https://github.com/MNagtegaal/SPIJN

Declaration of Competing Interest

The authors declare that there is no conflict of interest.

Credit authorship contribution statement

L. Nunez-Gonzalez: Conceptualization, Data curation, Formal analysis, Investigation, Methodology, Software, Project administration, Validation, Visualization, Writing – original draft, Writing – review & editing. **M.A. Nagtegaal:** Conceptualization, Data curation, Formal analysis, Methodology, Investigation, Software, Validation, Visualization, Writing – original draft, Writing – review & editing. **D.H.J. Poot:** Conceptualization, Data curation, Methodology, Software, Supervision, Writing – review & editing. **J. de Bresser:** Conceptualization, Funding acquisition, Supervision, Writing – review & editing. **M.J.P. van Osch:** Conceptualization, Supervision, Writing – review & editing. **J.A. Hernandez-Tamames:** Conceptualization, Funding acquisition, Methodology, Project administration, Resources, Supervision, Writing – review & editing. **F.M. Vos:** Conceptualization, Funding acquisition, Methodology, Project administration, Supervision, Writing – review & editing.

Data Availability

In vivo reconstructed data is publicly available at doi.org/10.5281/zenodo.5576039. The authors do not have permission to share data.

Acknowledgements

Supplementary materials

Supplementary material associated with this article can be found, in the online version, at doi:10.1016/j.neuroimage.2022.119638.

Appendix I

The acquired MRF data was reconstructed using an in-house created low-rank reconstruction algorithm, solving

$$P,\ U\ = \mathrm{argmin}_{P,U}\ \sum_{c,j} \left| S_{j,c} -\ F_j C_c P U_j \right|_2^2 +\ R(P)$$

where $P \in \mathbb{C}^{|\Omega_X| \times N}$ is a matrix containing the N low-rank component images of spatial dimension $|\Omega_X|$, which is the compressed representation of the MRF series; $P \in \Omega^{N \times 1000}$ contains the N time components based on which the MRF signal is compressed, i.e. the time-compression matrix, and $U_j \in \mathbb{C}^N$ is a particular column from this matrix for contrast weighting j (thus, $x = PU_j$ is the reconstructed contrast image j from the MRF series); $S_{j,c} \in \mathbb{C}^{|\Omega_j|}$ is the acquired undersampled data of MRF contrast weighting j of coil c; $C_c \in \mathbb{C}^{|\Omega_X| \times |\Omega_X|}$ is a diagonal matrix specifying the sensitivity of coil c; $F_j \in \mathbb{C}^{|\Omega_j| \times |\Omega_X|}$ represents the non-uniform Fast Fourier transform (Fessler and Sutton, 2003) for contrast weighting j. Furthermore, $R(P) =\ \sum_X \sqrt{\sum_i P_{x,i}^2}$, i.e. the spatial L1 norm of the L2 norm across the component images, is applied for regularization purposes.

The equation was solved by three iterations of a block coordinate descent optimization, alternating the optimization between U and P.

The initial time compression matrix U was constructed from the first 6 singular vectors obtained through SVD of a dictionary precomputed as described in 'Methods' in the subsection 'Single and multi-component parameter estimation'. After this, initial-images were created by subsequently applying to S_j: a density compensation, an adjoint non-uniform Fourier transformation, and a projection to the subspace with the initial U. Then, using the first subspace component derived from the initial-images, the cross-correlation matrix among the 12 acquired channels was computed for each voxel. The output was a matrix of 12 by 12 images which were filtered using a box blur filter of size 5, resulting in a modified correlation-among-channels matrix for each voxel. Each voxel of the coil sensitivity maps (C_c) was created from the first singular vector of its modified correlation-among-channels matrix. The initial P was created by the projection of the initial-images on C_c. In subsequent iterations the explicit least squares solution for U_j was computed followed by ortho-normalization. Subsequently, the subproblem for P was solved by the conjugate gradient algorithm, where R(P) was approximated by its tight quadratic overbound (Fan and Li, 2001).

References

Alonso-Ortiz, E., Levesque, I.R., Pike, G.B., 2015. MRI-based myelin water imaging: a technical review: MRI-based myelin water imaging. Magn. Reson. Med. 73, 70–81. doi:10.1002/mrm.25198.

Alonso-Ortiz, E., Levesque, I.R., Pike, G.B., 2018. Multi-gradient-echo myelin water fraction imaging: comparison to the multi-echo-spin-echo technique. Magn. Reson. Med. 79, 1439–1446. doi:10.1002/mrm.26809.

Ashburner, J., Friston, K.J., 2005. Unified segmentation. Neuroimage 26, 839–851. doi:10.1016/j.neuroimage.2005.02.018.

Ashburner, J., 2007. A fast diffeomorphic image registration algorithm. Neuroimage 38, 95–113. doi:10.1016/j.neuroimage.2007.07.007.

Aubert-Broche, B., Evans, A.C., Collins, L., 2006. A new improved version of the realistic digital brain phantom. Neuroimage 32, 138–145. doi:10.1016/j.neuroimage.2006.03.052.

Badve, C., Yu, A., Dastmalchian, S., Rogers, M., Ma, D., Jiang, Y., et al., 2017. MR fingerprinting of adult brain tumors: initial experience. Am. J. Neuroradiol. 38, 492–499. doi:10.3174/ajnr.A5035.

Bojorquez, J.Z., Bricq, S., Acquitter, C., Brunotte, F., Walker, P.M., Lalande, A., 2017. What are normal relaxation times of tissues at 3 T? Magn. Reson. Imaging 35, 69–80. doi:10.1016/j.mri.2016.08.021.

Bouhrara, M., Spencer, R.G., 2017. Rapid simultaneous high-resolution mapping of myelin water fraction and relaxation times in human brain using BMC-mcDESPOT. Neuroimage 147, 800–811. doi:10.1016/j.neuroimage.2016.09.064.

Buonincontri, G., Biagi, L., Retico, A., Cecchi, P., Cosottini, M., Gallagher, F.A., et al., 2019. Multi-site repeatability and reproducibility of MR fingerprinting of the healthy brain at 1.5 and 3.0 T. Neuroimage 195, 362–372. doi:10.1016/j.neuroimage.2019.03.047.

Cencini, M., Lancione, M., Biagi, L., Kurzawski, J.W., Pasquetiello, R., Donatelli, G., et al., 2021. Myelin water fraction mapping in developing children using magnetic resonance fingerprinting. In: Proceedings of the International Society for Magnetic Resonance in Medicine, 29. ISMRM, p. 0165 29.

Chen, Y., Chen, M.H., Baluyot, K.R., Potts, T.M., Jimenez, J., Lin, W., 2019. MR fingerprinting enables quantitative measures of brain tissue relaxation times and myelin water fraction in the first five years of life. Neuroimage 186, 782–793. doi:10.1016/j.neuroimage.2018.11.038.

Chen, Y., Jiang, Y., Pahwa, S., Ma, D., Lu, L., Twieg, M.D., et al., 2016. MR fingerprinting for rapid quantitative abdominal imaging. Radiology 279, 278–286. doi:10.1148/radiol.2016152037.

Crum, W.R., Camara, O., Hill, DLG., 2006. Generalized overlap measures for evaluation and validation in medical image analysis. IEEE Trans. Med. Imaging 25, 1451–1461. doi:10.1109/TMI.2006.880587.

Cruz, G., Jaubert, O., Schneider, T., Botnar, R.M., Prieto, C., 2019. Rigid motion-corrected magnetic resonance fingerprinting. Magn. Reson. Med. 81, 947–961. doi:10.1002/mrm.27448.

de Bresser, J., Portegies, M.P., Leemans, A., Biessels, G.J., Kappelle, L.J., Viergever, MA., 2011. A comparison of MR based segmentation methods for measuring brain atrophy progression. Neuroimage 54, 760–768. doi:10.1016/j.neuroimage.2010.09.060.

Deshmane, A., McGivney, D.F., Ma, D., Jiang, Y., Badve, C., Gulani, V., et al., 2019. Partial volume mapping using magnetic resonance fingerprinting. NMR Biomed. 32, e4082. doi:10.1002/nbm.4082.

Duarte, R., Repetti, A., Gómez, P.A., Davies, M., Wiaux, Y., 2020. Greedy approximate projection for magnetic resonance fingerprinting with partial volumes. Inverse Prob. 36, 035015. doi:10.1088/1361-6420/ab356d.

Dvorak, A.V., Ljungberg, E., Vavasour, I.M., Lee, L.E., Abel, S., Li, D.K.B., et al., 2021. Comparison of multi echo T 2 relaxation and steady state approaches for myelin imaging in the central nervous system. Sci. Rep. 11, 1–12. doi:10.1038/s41598-020-80585-7.

Dvorak, A.V., Swift-LaPointe, T., Vavasour, I.M., Lee, L.E., Abel, S., Russell-Schulz, B., et al., 2021. An atlas for human brain myelin content throughout the adult life span. Sci. Rep. 11, 1–13. doi:10.1038/s41598-020-79540-3.

Fan, J., Li, R., 2001. Variable selection via nonconcave penalized likelihood and its oracle properties. J. Am. Statist. Assoc. 96, 1348–1360. doi:10.1198/016214501753382273.

Fessler, J.A., Sutton, B.P., 2003. Nonuniform fast fourier transforms using min-max interpolation. IEEE Trans. Signal Process. 51, 560–574. doi:10.1109/TSP.2002.807005.

Fonov, V., Evans, A., McKinstry, R., Almli, C., Collins, D., 2009. Unbiased nonlinear average age-appropriate brain templates from birth to adulthood. Neuroimage 47, S102. doi:10.1016/S1053-8119(09)70884-5.

Fonov, V., Evans, A.C., Botteron, K., Almli, C.R., McKinstry, R.C., Collins, D.L., 2011. Unbiased average age-appropriate atlases for pediatric studies. Neuroimage 54, 313–327. doi:10.1016/j.neuroimage.2010.07.033.

Giorgio, A., De Stefano, N., 2013. Clinical use of brain volumetry. J. Magn. Reson. Imaging 37, 1–14. doi:10.1002/jmri.23671.

Heesterbeek, D.G.J., Vos, F., Gijzen van, M., Nagtegaal, M.A., 2021. Sequence optimisation for multi-component analysis in magnetic resonance fingerprinting. In: Proceedings of the International Society for Magnetic Resonance in Medicine, 29. ISMRM, p. 1561 vol. 292021.

Heinen, R., Bouvy, W.H., Mendrik, A.M., Viergever, M.A., Biessels, G.J., de Bresser, J., 2016. Robustness of automated methods for brain volume measurements across different MRI field strengths. PLoS One 11, e0165719. doi:10.1371/journal.pone.0165719.

Hennig, J., 1988. Multiecho imaging sequences with low refocusing flip angles. J. Magn. Reson. 78, 397–407. doi:10.1016/0022-2364(88)90128-X.

Jaubert, O., Cruz, G., Bustin, A., Schneider, T., Lavin, B., Koken, P., et al., 2020. Water–fat dixon cardiac magnetic resonance fingerprinting. Magn. Reson. Med. 83, 2107–2123. doi:10.1002/mrm.28070.

Jenkinson, M., Beckmann, C.F., Behrens, T.E.J., Woolrich, M.W., Smith, S.M., 2012. FSL. Neuroimage 62, 782–790. doi:10.1016/j.neuroimage.2011.09.015.

Jiang, Y., Ma, D., Seiberlich, N., Gulani, V., Griswold, MA., 2015. MR fingerprinting using fast imaging with steady state precession (FISP) with spiral readout. Magn. Reson. Med. 74, 1621–1631. doi:10.1002/mrm.25559.

Johnson, K.O., Robison, R.K., Pipe, J.G., 2011. Rigid body motion compensation for spiral projection imaging. IEEE Trans. Med. Imaging 30, 655–665. doi:10.1109/TMI.2010.2091146.

Kim, D., Wisnowski, J.L., Nguyen, C.T., Haldar, JP., 2022. Multidimensional correlation spectroscopic imaging of exponential decays: From theoretical principles to *in vivo* human applications. NMR Biomed. e4244. doi:10.1002/nbm.4244, n.d.;n/a.

Klauschen, F., Goldman, A., Barra, V., Meyer-Lindenberg, A., Lundervold, A., 2009. Evaluation of automated brain MR image segmentation and volumetry methods. Hum. Brain Mapp. 30, 1310–1327. doi:10.1002/hbm.20599.

Kolind, S., Seddigh, A., Combes, A., Russell-Schulz, B., Tam, R., Yogendrakumar, V., et al., 2015. Brain and cord myelin water imaging: a progressive multiple sclerosis biomarker. NeuroImage Clin. 9, 574–580. doi:10.1016/j.nicl.2015.10.002.

Körzdörfer, G., Kirsch, R., Liu, K., Pfeuffer, J., Hensel, B., Jiang, Y., et al., 2019. Reproducibility and repeatability of MR fingerprinting relaxometry in the human brain. Radiology, 182360 doi:10.1148/radiol.2019182360.

Kurzawski, J.W., Cencini, M., Peretti, L., Gómez, P.A., Schulte, R.F., Donatelli, G., et al., 2022. Retrospective rigid motion correction of three-dimensional magnetic resonance fingerprinting of the human brain. Magn. Reson. Med. doi:10.1002/mrm.28301, n.d.;n/a.

Laule, C., Kozlowski, P., Leung, E., Li, D.K.B., MacKay, A.L., Moore, GRW., 2008. Myelin water imaging of multiple sclerosis at 7 T: correlations with histopathology. Neuroimage 40, 1575–1580. doi:10.1016/j.neuroimage.2007.12.008.

Laule, C., Leung, E., Li, D.K., Traboulsee, A.L., Paty, D.W., MacKay, A.L., et al., 2006. Myelin water imaging in multiple sclerosis: quantitative correlations with histopathology. Mult. Scler 12, 747–753. doi:10.1177/1352458506070928.

Ma, D., Gulani, V., Seiberlich, N., Liu, K., Sunshine, J.L., Duerk, J.L., et al., 2013. Magnetic resonance fingerprinting. Nature 495, 187–192. doi:10.1038/nature11971.

Mackay, A., Whittall, K., Adler, J., Li, D., Paty, D., Graeb, D., 1994. *In vivo* visualization of myelin water in brain by magnetic resonance. Magn. Reson. Med. 31, 673–677. doi:10.1002/mrm.1910310614.

McGivney, D., Deshmane, A., Jiang, Y., Ma, D., Badve, C., Sloan, A., et al., 2018. Bayesian estimation of multicomponent relaxation parameters in magnetic resonance fingerprinting: bayesian MRF. Magn. Reson. Med. 80, 159–170. doi:10.1002/mrm.27017.

McMillan, K., Uike, M., Tao, X., Okuda, H., Healthcare, G., 2022. MR efficiency becomes critical as healthcare costs. Scanner Time Demand Increases 4 n.d..

Mehta, B.B., Ma, D., Pierre, E.Y., Jiang, Y., Coppo, S., Griswold, M.A., 2018. Image reconstruction algorithm for motion insensitive MR Fingerprinting (MRF): MORF. Magnetic Resonance in. Medicine 80, 2485–2500. doi:10.1002/mrm.27227, (Baltimore).

Nagtegaal, M.A., Koken, P., Amthor, T., Doneva, M., 2020. Fast multi-component analysis using a joint sparsity constraint for MR fingerprinting. Magn. Reson. Med. 83, 521–534. doi:10.1002/mrm.27947.

Nunez-Gonzalez, L., Kotek, G., Gómez, P.A., Buonincontri, G., Vogel, M., Krestin, G.P., et al., 2021. Accuracy and repeatability of QRAPMASTER and MRF-vFA. Magn. Reson. Imaging 83, 196–207. doi:10.1016/j.mri.2021.09.004.

Piredda, G.F., Hilbert, T., Thiran, J.P., Kober, T., 2021. Probing myelin content of the human brain with MRI: a review. Magn. Reson. Med. 85, 627–652. doi:10.1002/mrm.28509.

Pirkl, C.M., Nunez-Gonzalez, L., Kofler, F., Endt, S., Grundl, L., Golbabaee, M., et al., 2021. Accelerated 3D whole-brain T1, T2, and proton density mapping: feasibility for clinical glioma MR imaging. Neuroradiology doi:10.1007/s00234-021-02703-0.

Ross, DE., 2011. Review of longitudinal studies of MRI brain volumetry in patients with traumatic brain injury. Brain Inj. 25, 1271–1278. doi:10.3109/02699052.2011.624568.

Ryu, K.H., Baek, H.J., Moon, J.I., Choi, B.H., Park, S.E., Ha, J.Y., et al., 2020. Initial clinical experience of synthetic MRI as a routine neuroimaging protocol in daily practice: a single-center study. J. Neuroradiol. 47, 151–160. doi:10.1016/j.neurad.2019.03.002.

SPM12 - Statistical parametric mapping n.d. https://www.fil.ion.ucl.ac.uk/spm (accessed October 13, 2019).

Stanisz, G.J., Odrobina, E.E., Pun, J., Escaravage, M., Graham, S.J., Bronskill, M.J., et al., 2005. T1, T2 relaxation and magnetization transfer in tissue at 3T. Magn. Reson. Med. 54, 507–512. doi:10.1002/mrm.20605.

Su, P., Mao, D., Liu, P., Li, Y., Pinho, M.C., Welch, B.G., et al., 2017. Multiparametric estimation of brain hemodynamics with MR fingerprinting ASL: MRFingerprintingASL. Magn Reson Med 78, 1812–1823. doi:10.1002/mrm.26587.

Tang, S., Fernandez-Granda, C., Lannuzel, S., Bernstein, B., Lattanzi, R., Cloos, M., et al., 2018. Multicompartment magnetic resonance fingerprinting. Inverse Prob. 34, 094005. doi:10.1088/1361-6420/aad1c3.

Tudorascu, D.L., Karim, H.T., Maronge, J.M., Alhilali, L., Fakhran, S., Aizenstein, H.J., et al., 2016. Reproducibility and bias in healthy brain segmentation: comparison of two popular neuroimaging platforms. Front. Neurosci. 10. doi:10.3389/fnins.2016.00503.

Warntjes, J.B.M., Leinhard, O.D., West, J., Lundberg, P., 2008. Rapid magnetic resonance quantification on the brain: optimization for clinical usage. Magn. Reson. Med. 60, 320–329. doi:10.1002/mrm.21635.

Weigel, M., 2015. Extended phase graphs: Dephasing, RF pulses, and echoes - pure and simple: extended phase graphs. J. Magn. Reson. Imaging 41, 266–295. doi:10.1002/jmri.24619.

Whittall, K.P., Mackay, A.L., Graeb, D.A., Nugent, R.A., Li, D.K.B., Paty, D.W., 1997. *In vivo* measurement ofT2 distributions and water contents in normal human brain. Magn. Reson. 37, 34–43. doi:10.1002/mrm.1910370107.

Yu, Z., Zhao, T., Assländer, J., Lattanzi, R., Sodickson, D.K., Cloos, MA., 2018. Exploring the sensitivity of magnetic resonance fingerprinting to motion. Magn. Reson. Imaging 54, 241–248. doi:10.1016/j.mri.2018.09.002.

Zhang, Y., Brady, M., Smith, S., 2001. Segmentation of brain MR images through a hidden Markov random field model and the expectation-maximization algorithm. IEEE Trans. Med. Imaging 20, 45–57. doi:10.1109/42.906424.